Title

Platinum-Anchored Iron Oxide Nanostructures for Efficient Hydrogen Evolution Reaction in Acidic Media

Journal

The Journal of Physical Chemistry C, 127(8)

ISSN

1932-7447

Authors

Yu, Bingzhe

Liu, Qiming

Nichols, Forrest

et al.

Publication Date

2023-03-02

DOI

10.1021/acs.jpcc.2c09033

THE JOURNAL OF PHYSICAL CHEMISTRY C
A JOURNAL OF THE AMERICAN CHEMICAL SOCIETY

pubs.acs.org/JPCC

Article

Platinum-Anchored Iron Oxide Nanostructures for Efficient Hydrogen Evolution Reaction in Acidic Media

Published as part of The Journal of Physical Chemistry virtual special issue "Zhao-Wu Tian Festschrift".

Bingzhe Yu, Qiming Liu, Forrest Nichols, Kiley Mayford, Dingjie Pan, Han-Lin Kuo, Jennifer Q. Lu, Frank Bridges, and Shaowei Chen*

Cite This: *J. Phys. Chem. C* 2023, 127, 3996–4005

Read Online

ACCESS | Metrics & More | Article Recommendations | Supporting Information

ABSTRACT: Metal oxides have been attracting extensive interest in the design and engineering of effective electrocatalysts owing to their unique electronic structure and natural abundance. However, the limited electrical conductivity and sluggish electron-transfer kinetics have hampered their widespread applications. These issues can be mitigated by structural engineering with the incorporation of select precious metal species. Herein, iron oxide nanostructures decorated with platinum species are prepared by the facile thermal annealing of a MIL-101 precursor along with the addition of a controlled amount of $PtCl_4$ and exhibit apparent electrocatalytic activity toward the hydrogen evolution reaction in 0.5 M H_2SO_4. The best sample needs only an ultralow overpotential of −15 mV to reach the current density of 10 mA cm^{-2}, along with a low Tafel slope of 25.4 mV dec^{-1}, a performance markedly better than that of commercial 20 wt % Pt/C. This is ascribed to the synergistic interactions between the Pt and Fe_2O_3 scaffold that impact the material's electrical conductivity and electron-transfer kinetics and the Cl residuals that regulate the adsorption free energy of H, as confirmed in computational studies based on density functional theory. Results from this study highlight the unique potential of metal oxide-based nanocomposites as high-performance, low-cost electrocatalysts for electrochemical energy technologies where the performance can be further regulated by anion residuals.

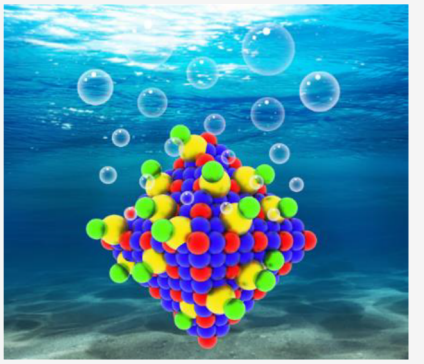

INTRODUCTION

With the rapid depletion of conventional energy sources and the environmental impacts arising from the combustion of fossil fuels, the development of sustainable energy technologies has been attracting increasing attention.[1−4] Within this context, hydrogen (H_2) has been hailed as a unique alternative energy source thanks to its zero-carbon emission and high gravimetric energy density.[5−8] The hydrogen evolution reaction (HER), a crucial half-reaction of water splitting, serves as a key technology for hydrogen production,[9,10] and platinum-based nanomaterials have been used as state-of-the-art catalysts for HER.[11] However, the high cost and scarcity of platinum greatly impede large-scale applications.[12,13] To mitigate these issues, one effective strategy is to develop high-performance HER catalysts with a minimal amount of platinum. This can be achieved by dispersing Pt within a select structural scaffold, such as carbon derivatives, transition-metal oxides, and metal nanoparticles, among others.[14] For example, Wu et al.[15] anchored Pt clusters onto $Ti_3C_2T_x$ MXene and observed a low overpotential (η_{10}) of −34 mV to reach the current density of 10 mA cm^{-2} in 0.5 M H_2SO_4, and the HER activity was accounted for by the oxygen and fluorine terminal groups of MXene that weakened the adsorption of hydrogen on Pt. A similar performance was reported by Kuang et al.,[16] where they immobilized Pt species onto N-doped hollow carbon spheres and observed an η_{10} of −40 mV, due to the electronic interactions between the Pt single atoms and the carbon scaffold.

Metal oxide-supported catalysts have also been attracting particular interest largely because of the ready availability and wide range of oxide scaffolds, their unique electrochemical activity, and synergistic interactions with metal dopants. For instance, Zhou et al.[17] embedded Pt single atoms in NiO/Ni nanosheets supported on a Ag nanowire network, which exhibited a remarkable HER activity (η_{10} = −26 mV) in 1 M KOH due to the preferred adsorption of both OH* and H* on metallic Ni and oxygen vacancy-modified NiO active sites. Wang et al.[18] immobilized Pt atomic species onto monolayer WO_3 nanosheets via a hydrothermal and pyrolytic method and observed a low η_{10} of −22 mV in 0.5 M H_2SO_4, which was ascribed to the strong synergetic interactions between the Pt

Received: December 26, 2022
Revised: January 29, 2023
Published: February 9, 2023

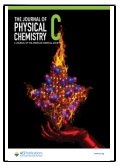

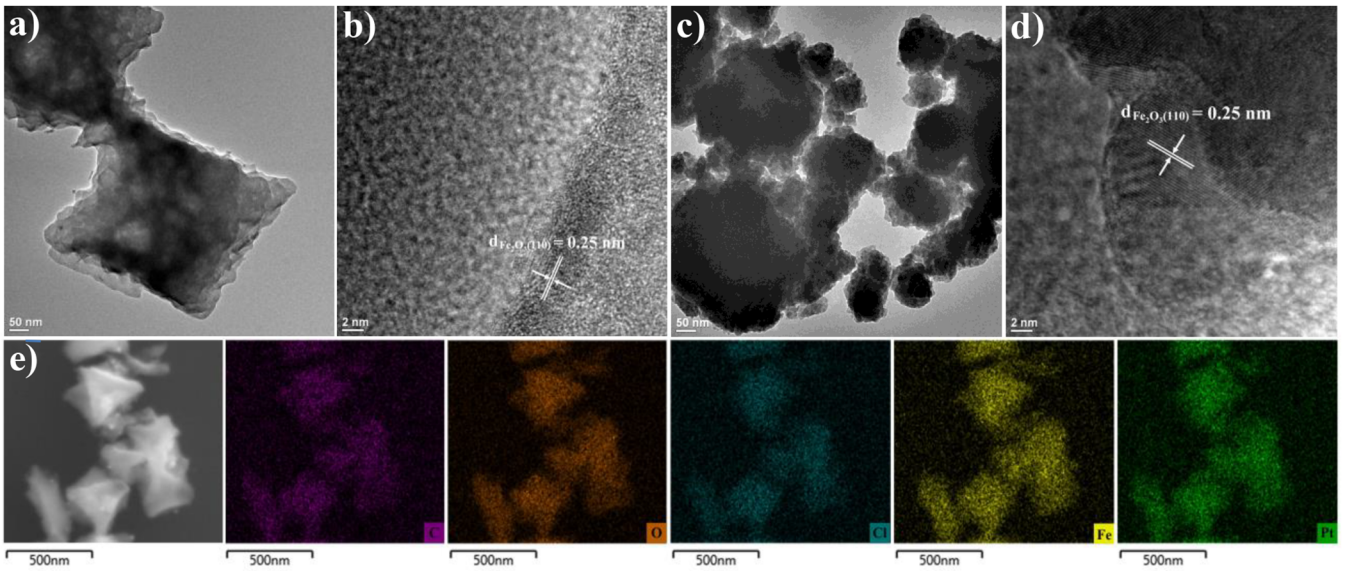

Figure 1. TEM images of (a, b) Fe_2O_3 and (c, d) Pt_5/Fe_2O_3. (e) SEM image and elemental maps of C, O, Cl, Fe, and Pt of Pt_5/Fe_2O_3. Scale bars are (a) 50, (b) 2, (c) 50, (d) 2, and (e) 500 nm.

single atoms and WO_3 support. Such metal−support interactions were also found to dictate the HER activity of nanocomposites with subnanometer-sized PtO_x clusters supported on TiO_2,[19] which featured an η_{10} of −125 mV in 0.5 M H_2SO_4.

Notably, in these previous studies, metal chlorides (e.g., $PtCl_4$ and H_2PtCl_6) were used extensively as the precursors, and the final products typically consisted of a non-negligible number of anion residuals. Yet, their impacts on the HER performance were largely unexplored. In a series of recent studies,[20−22] it has been demonstrated that the anion residuals can significantly impact the electronic properties of the catalytic active sites, the interactions with key reaction intermediates, and ultimately the electrocatalytic performance. That is, the anion residuals can also be exploited as a unique variable to manipulate the electrocatalytic activity of the functional nanocomposites.

Herein, we report a facile procedure to prepare platinum-anchored iron oxide nanostructures (Pt_x/Fe_2O_3) by thermally annealing MIL-101 along with the addition of a calculated amount (x) of $PtCl_4$ in a muffle furnace. The incorporation of Pt onto the iron oxide scaffold markedly improves the HER activity in acidic media, and the best sample exhibits an ultralow η_{10} of only −15 mV and a Tafel slope of 25.4 mV dec^{-1}, along with remarkable cycling stability. Such performance is markedly better than that of commercial Pt/C and relevant catalysts reported recently in the literature. This is ascribed to the synergistic interactions between Pt and the Fe_2O_3 scaffold that enhance the material's electrical conductivity and charge-transfer kinetics as well as Cl residuals that impacted the electronic properties of the Pt centers and hence the adsorption of H, as confirmed by results from density functional theory (DFT) calculations.

EXPERIMENTAL SECTION

Chemicals. Ferric chloride hexahydrate ($FeCl_3{\cdot}6H_2O$, Fisher Chemicals), platinum(IV) chloride ($PtCl_4$, 99%, Acros Organics), Pt/C (20 wt %, Alfa Aesar), *N*,*N*-dimethylformamide (DMF, Fisher Chemicals), terephthalic acid ($(C_6H_4(COOH)_2$, 99%, Acros Organics), Nafion 117 solution (95%, Aldrich), 2-propanol (HPLC grade, Fisher Chemicals), and sulfuric acid (H_2SO_4, 98%, Fisher Chemicals) were used as received. Deionized water was obtained from a Barnstead Nanopure water system (18.3 MΩ cm).

Sample Preparation. MIL-101 was prepared by adopting a protocol reported previously.[23] Briefly, 8 mmol of $FeCl_3{\cdot}6H_2O$ and 4 mmol of terephthalic acid were dissolved in 60 mL of DMF under magnetic stirring at room temperature. The solution was then transferred into a 100 mL Teflon-lined stainless steel autoclave and held at 120 °C for 24 h, producing an orange precipitate which was collected by centrifugation and rinsed with DMF three times before being dried under vacuum at 60 °C for 12 h.

The MIL-101 (100 mg) prepared above was then dispersed in 50 mL of deionized water under sonication for 15 min, followed by the addition of a series of $PtCl_4$ solutions at various concentrations (i.e., x = 0.5, 1, 2, 5, and 10 mmol L^{-1}) under magnetic stirring for 3 h at room temperature. The precipitates were collected by centrifugation, dried under vacuum at 50 °C for 12 h, and referred to as Pt_x/MIL-101.

A certain quantity (50 mg) of the MIL-101 or Pt_x/MIL-101 obtained above was loaded onto a ceramic boat, which was placed in a muffle furnace and held at 300 °C for 4 h in the air. The resulting powders were iron oxide nanostructures decorated with various amounts of Pt and denoted as Fe_2O_3, $Pt_{0.5}/Fe_2O_3$, Pt_1/Fe_2O_3, Pt_2/Fe_2O_3, Pt_5/Fe_2O_3, and Pt_{10}/Fe_2O_3, respectively.

Characterization. Transmission electron microscopy (TEM) images were acquired with a Tecni G2 operated at 200 kV. Scanning electron microscopy (SEM) and energy-dispersive spectroscopic (EDS) mapping studies were carried out with an Apreo SEM microscope. X-ray diffraction (XRD) patterns were collected with a Bruker D8 Advance diffractometer using Cu K_α radiation (λ = 0.15418 nm). Raman measurements were carried out with a Horiba Jobin Yvon LabRAM ARAMIS automated scanning confocal Raman microscope under 532 nm excitation. X-ray photoelectron spectra (XPS) were collected with a Thermo Fisher K-Alpha

https://doi.org/10.1021/acs.jpcc.2c09033
J. Phys. Chem. C 2023, 127, 3996−4005

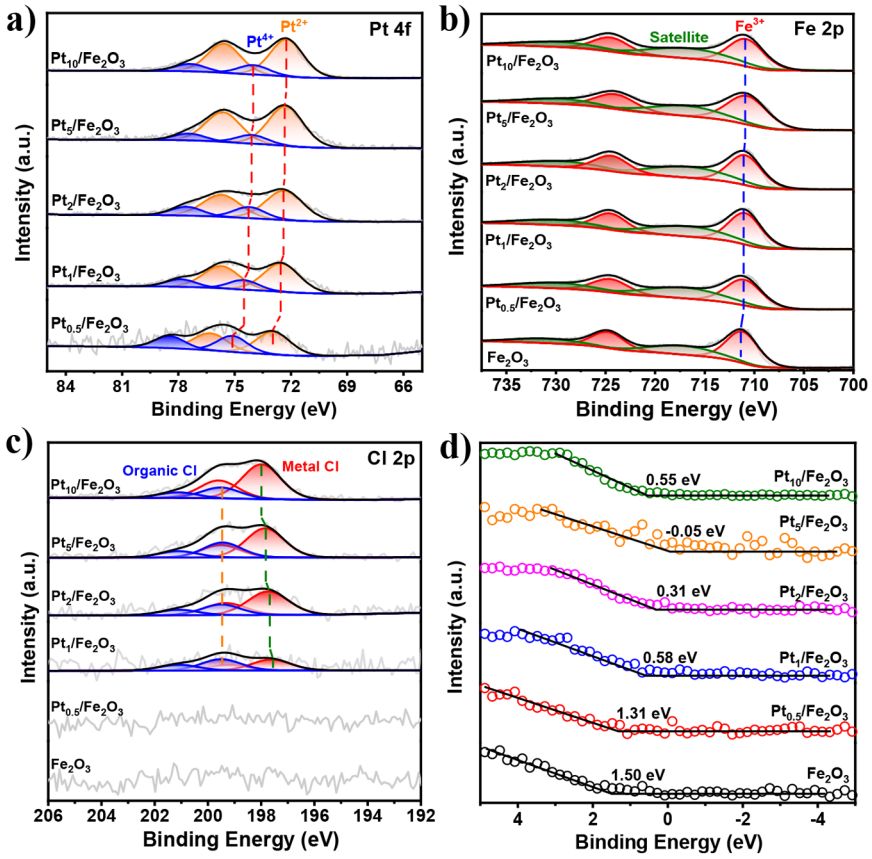

Figure 2. High-resolution XPS spectra of the (a) Pt 4f, (b) Fe 2p, and (c) Cl 2p electrons and (d) VBM profiles of Fe_2O_3, $Pt_{0.5}/Fe_2O_3$, Pt_1/Fe_2O_3, Pt_2/Fe_2O_3, Pt_5/Fe_2O_3, and Pt_{10}/Fe_2O_3.

system with the binding energy calibrated against the C 1s electrons. X-ray absorption spectroscopy (XAS) measurements were conducted at 10 K at beamline 4-1 of the Stanford Synchrotron Radiation Lightsource using an Oxford liquid helium cryostat. The contents of metal elements in the catalysts were evaluated by inductively coupled plasma-optical emission spectroscopy (ICP-OES) measurements with a PerkinElmer Optima instrument.

Electrochemical Measurements. The electrochemical performance was examined with a CHI 710 electrochemical workstation in a three-electrode configuration using a Ag/AgCl reference electrode, a graphite rod counter electrode, and a glassy carbon disk working electrode (surface area 0.196 cm^2). The reference electrode was calibrated against a reversible hydrogen electrode (RHE), and all potentials in the present study were referenced to the RHE. The catalyst inks were prepared by dispersing 2 mg of the samples prepared above along with 8 mg of carbon black into a mixed solution containing 740 μL of isopropanol, 250 μL of H_2O, and 10 μL of Nafion under sonication for 30 min. Then 20 μL of the inks was dropcast onto a glassy carbon disk electrode surface and dried naturally at room temperature before being coated with 5 μL of 20 wt % Nafion. The catalyst loading was 0.204 mg cm^{-2}. The HER polarization curves were collected in 0.5 M H_2SO_4 at a scan rate of 10 mV s^{-1} with the correction of *i*R compensation, and the electrode double-layer capacitance was quantified by cyclic voltammetric (CV) measurements in the non-Faradaic potential range. Electrochemical impedance spectroscopy (EIS) measurements were performed within the frequency range of 0.1 to 10^5 Hz at the AC amplitude of 5 mV. Chronopotentiometric measurements were conducted at a current density of 10 mA cm^{-2} for 30 000 s.

RESULTS AND DISCUSSION

The sample structures were first characterized by XRD measurements. From Figure S1, it can be seen that all samples exhibited only a featureless profile, suggesting the formation of a largely amorphous/nanocrystalline structure. In TEM measurements (Figure 1a–d and Figures S2–S7), one can see that all samples roughly retained the octahedral morphology of the starting MIL-101 after thermal annealing, with a lateral length of ca. 600 nm, but exhibited only an amorphous background embedded with nanocrystalline particles up to a few tens of nanometers in size, which featured an interplanar spacing of 0.25 nm that can be ascribed to the (110) planes of Fe_2O_3 (PDF 33-0664).[24,25] This suggests the successful conversion of MIL-101 to nanocrystalline hematite. In addition, no obvious features can be resolved for Pt or PtO_x, likely due to the atomic dispersion of Pt within the Fe_2O_3 scaffold. In elemental mapping analysis based on energy-dispersive X-ray spectroscopy (EDS) (Figure 1e), one can indeed see a homogeneous distribution of the C, O, Cl, Fe, and Pt elements, with Pt being far more discrete than Fe and O (Figure S8).

Consistent results were obtained from Raman measurements. From Figure S9, one can see that all samples possessed five major vibrational bands within the range of 100 to 700 cm^{-1} that can be ascribed to the A_{1g} modes (211 and 480 cm^{-1}) and E_g modes (270, 382, and 581 cm^{-1}) of hematite

https://doi.org/10.1021/acs.jpcc.2c09033
J. Phys. Chem. C 2023, 127, 3996−4005

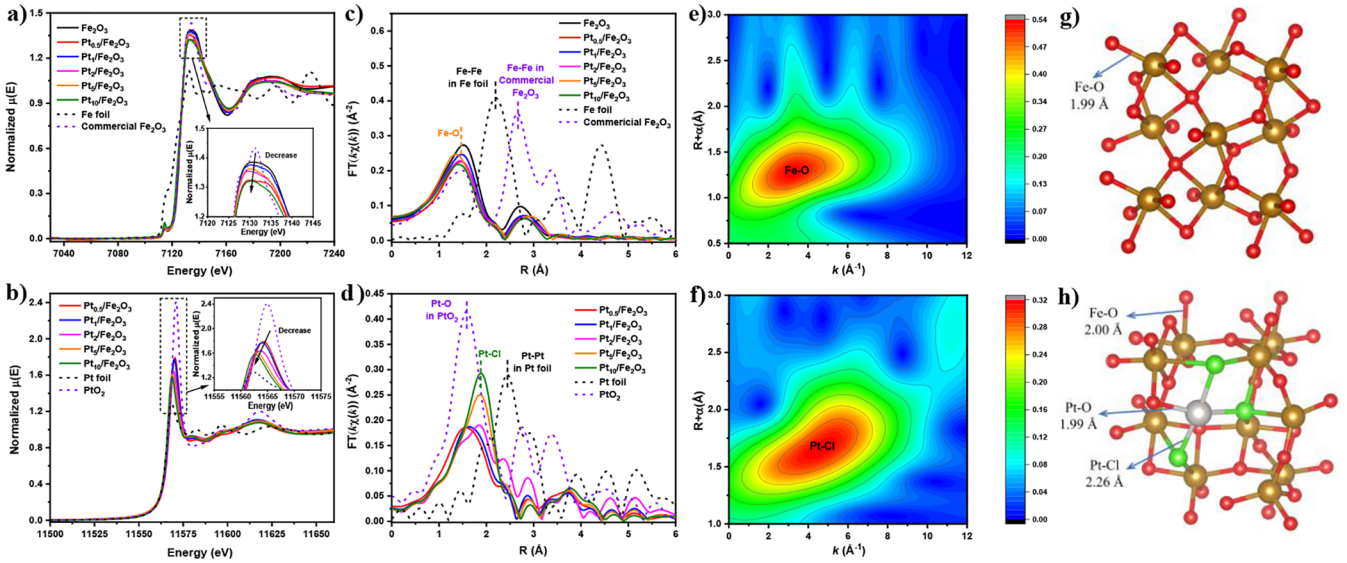

Figure 3. (a) Fe K-edge and (b) Pt L_3-edge XANES spectra. (c) Fourier transforms of the EXAFS spectra of the sample series, Fe foil, and commercial Fe_2O_3. (d) Fourier transforms of EXAFS spectra of the sample series, Pt foil, and PtO_2. (e) Fe K-edge and (f) Pt L_3-edge WT-EXAFS of Pt_5/Fe_2O_3. Ball-and-stick structural models of (g) Fe_2O_3 and (h) Pt_5/Fe_2O_3, with red for O, gold for Fe, silver for Pt, and green for Cl.

Fe_2O_3.[26,27] Yet, it can be seen that in comparison to the standard spectra of Fe_2O_3,[28] these vibrational bands all exhibited a slight red shift of the wavenumbers, likely due to the mostly amorphous structure of the samples.[29] The metal contents were then evaluated by ICP-OES measurements. From Table S1, it can be seen that the Pt loading increased with the increasing initial feed, $Pt_{0.5}/Fe_2O_3$ (0.70 wt %) < Pt_1/Fe_2O_3 (2.84 wt %) < Pt_2/Fe_2O_3 (9.69 wt %) < Pt_5/Fe_2O_3 (19.93 wt %) < Pt_{10}/Fe_2O_3 (26.17 wt %), in good agreement with that from EDS measurements (Figure S10). However, the Fe contents were all below the stoichiometric expectation of Fe_2O_3 but increased with the Pt feed. This may be ascribed to the formation of a mostly amorphous structure where the incorporation of the Pt species appeared to facilitate the thermal generation of Fe_2O_3 nanostructures, likely because of increasing consumption of carbon in the reduction of the platinum species at elevated temperatures (vide infra).

XPS measurements were then performed to investigate the elemental composition and valence state of the samples. Figure S11 shows the survey spectra of the sample series, where the Fe 2p, O 1s, Pt 4d, C 1s, Cl 2s, Cl 2p, Pt 4f, and Fe 3p electrons can be readily identified for all samples at ca. 724, 531, 316, 285, 269, 200, 76, and 56 eV, respectively (no Pt signals for the Fe_2O_3 sample). From the integrated peak areas, the elemental contents were then evaluated and are listed in Tables S2 and S3, where the Pt contents can be seen to be rather consistent with those from ICP-OES measurements (Table S1). In addition, the samples all contained a substantial amount of carbon derived from the MIL-101 precursor that diminished markedly with the Pt feed (Figure S12 and Table S2), again suggesting that the Pt species facilitated the thermal transformation of MIL-101 to Fe_2O_3. Figure 2a shows the high-resolution scans of the Pt 4f electrons which can all be deconvoluted into two doublets. The lower-energy pair at ca. 72.3/75.7 eV can be ascribed to the $4f_{7/2}/4f_{5/2}$ electrons of Pt^{2+}, whereas the higher-energy one at ca. 74.2/77.6 eV to those of Pt^{4+} (Table S4).[30,31] Additionally, the fact that the Pt^{2+}/Pt^{4+} atomic ratio increased, and concurrently the carbon contents diminished (Table S2), with increasing Pt loading suggests partial reduction of the $PtCl_4$ precursor during thermal annealing to Pt^{2+} most likely by carbon at elevated temperatures. Indeed, one can see that the Pt 4f binding energies exhibited a clear red shift (by ca. 0.6 eV for Pt^{2+} and 1.0 eV for Pt^{4+}) from $Pt_{0.5}/Fe_2O_3$ to Pt_{10}/Fe_2O_3 (Table S4), indicating an increasing electron density of the Pt species in the samples, most likely due to electron transfer from the reducing carbon (with additional contributions from residual Cl, vide infra).

The corresponding Fe 2p spectra are shown in Figure 2b, where it can be seen that all samples possessed a doublet at the binding energies of 711.0/724.7 eV due to the $2p_{2/3}/2p_{1/2}$ electrons of Fe^{3+} species, with the corresponding satellite peaks located at 717.1 and 729.5 eV (Table S4).[32,33] Additionally, the Fe 2p binding energies also exhibit a slight red shift with increasing Pt loading in the sample by ca. 0.3 eV from Fe_2O_3 to Pt_{10}/Fe_2O_3, again likely arising from electron transfer from the reducing carbon.

Figure 2c shows the Cl 2p spectra of the sample series. One can see that no Cl species could be resolved in Fe_2O_3 and $Pt_{0.5}/Fe_2O_3$, whereas the other samples entail two doublets, the first one at 197.99/199.59 eV due to metal−Cl and the other at 199.51/201.11 eV to organic Cl (Table S5).[21] This suggests that the metal−Cl species arose primarily from the incomplete decomposition of the $PtCl_4$ precursor and mostly involved Cl bonded to Pt. Interestingly, whereas the organic Cl binding energy remained largely unchanged, the Pt−Cl species showed a clear increase in binding energy with increasing Pt loading by ca. 0.3 eV from $Pt_{0.5}/Fe_2O_3$ to Pt_{10}/Fe_2O_3, suggesting enhanced charge transfer from Cl to Pt (Table S5).

The corresponding O 1s spectra are shown in Figure S13, where all samples can be seen to contain a metal−O peak at ca. 530 eV (in addition to C═O at 531.2 eV and C−O at 533.1 eV), in good agreement with the formation of metal oxides by thermal annealing of MIL-101 and $PtCl_4$. Note that whereas the peak at ca. 531 eV has been assigned to oxygen vacancies in some earlier studies,[34,35] electron paramagnetic resonance (EPR) measurements of the Pt/Fe_2O_3 samples exhibited only

https://doi.org/10.1021/acs.jpcc.2c09033
J. Phys. Chem. C 2023, 127, 3996−4005

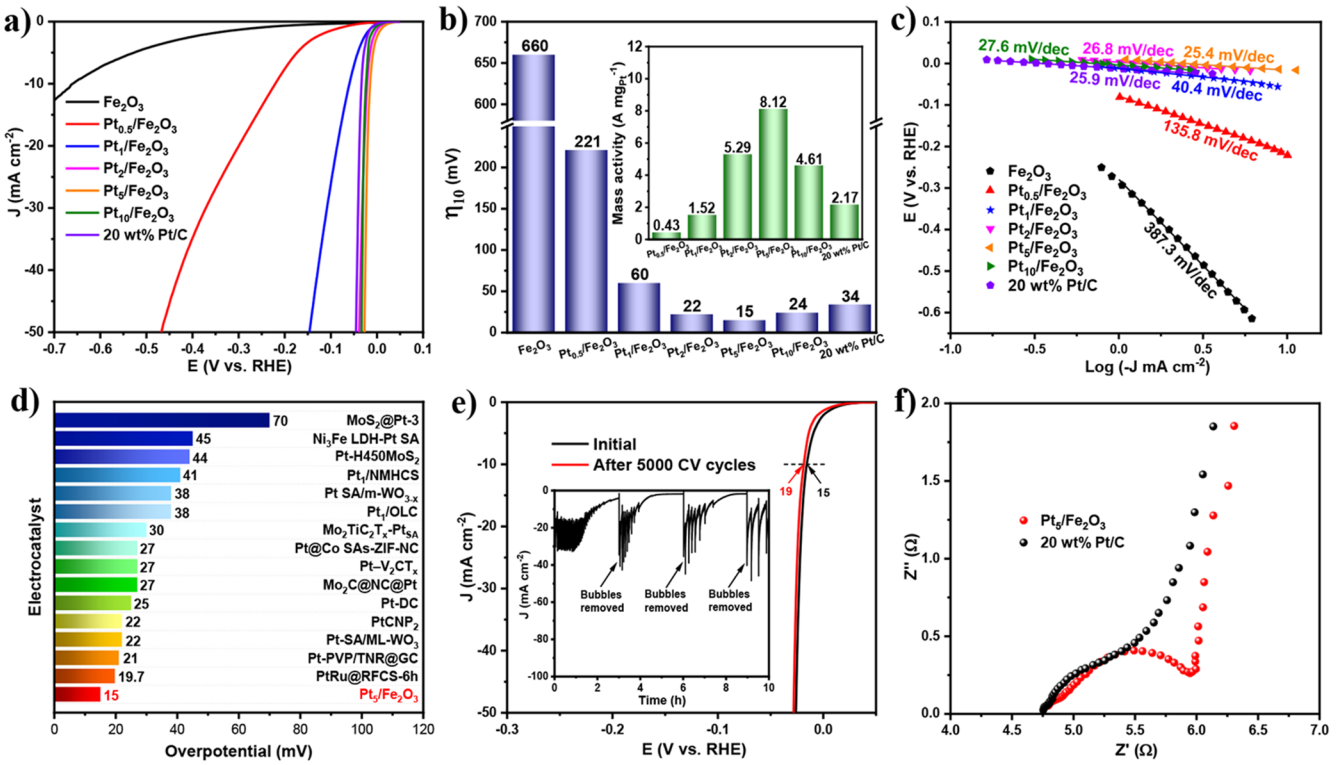

Figure 4. (a) HER polarization curves, (b) comparison of η_{10} (inset is the mass activity at the overpotential of −50 mV), and (c) Tafel slopes of Fe_2O_3, $Pt_{0.5}/Fe_2O_3$, Pt_1/Fe_2O_3, Pt_2/Fe_2O_3, Pt_5/Fe_2O_3, Pt_{10}/Fe_2O_3, and 20 wt % Pt/C in 0.5 M H_2SO_4. (d) Comparison of η_{10} between Pt_5/Fe_2O_3 and other state-of-the-art Pt-based electrocatalysts. (e) HER polarization curves of Pt_5/Fe_2O_3 before and after 5000 CV cycles. The inset is the current−time profile of Pt_5/Fe_2O_3 at the overpotential of −40 mV for 10 h, with hydrogen bubbles shaken off at the third, sixth, and ninth hours. (f) Nyquist plots of Pt_5/Fe_2O_3 and 20 wt % Pt/C at the overpotential of −10 mV.

featureless profiles, ruling out the formation of oxygen vacancies in the samples (not shown).

Figure 2d shows the valence band maximum (VBM) profiles of the sample series, where the Pt-free Fe_2O_3 can be seen to exhibit the lowest VBM at 1.50 eV, which was then up-shifted markedly upon Pt loading to 1.31 eV for $Pt_{0.5}/Fe_2O_3$, 0.58 eV for Pt_1/Fe_2O_3, and 0.31 eV for Pt_2/Fe_2O_3 and became negative at −0.05 eV for Pt_5/Fe_2O_3 before bouncing back to 0.55 eV for Pt_{10}/Fe_2O_3. That is, the incorporation of Pt into Fe_2O_3 led to an apparent change in the nanocomposite electrical conductivity, where Pt_5/Fe_2O_3 actually behaved like a conductor (with a negative VBM), whereas others were mostly semiconducting (with a positive VBM).[36] In addition, one can see that the VBM of Pt_5/Fe_2O_3 was the closest to the Fermi level, suggesting the highest activity in electron-transfer reactions. Such an apparent difference of the intrinsic electronic properties led to a marked differentiation of their electrocatalytic activity (vide infra).[37]

Consistent structural insights were obtained from XAS measurements. From the Fe K-edge X-ray absorption near-edge structure (XANES) spectra in Figure 3a, it can be seen that the absorption edge of the sample series was very close to that of commercial Fe_2O_3 but deviated markedly from that of the Fe foil (Figure S14a), indicating that the Fe valence state in the samples was close to +3, in good agreement with the results from XPS measurements (Figure 2b). Additionally, one can see that the white line intensity diminished somewhat with increasing Pt loading in the sample (Figure 3a inset), suggesting a slightly decreasing valence state of the Fe centers. This is in accord with the slight red shift of the Fe 2p binding energy (Figure 2b).

The corresponding Pt L_3-edge XANES are shown in Figure 3b, where the absorption edge of the sample series can be found to be situated between those of the Pt foil and PtO_2 (Figure S14b), suggesting that the Pt valence state was between 0 and +4 and the average valence state diminished in the order of $Pt_{0.5}/Fe_2O_3$ > Pt_1/Fe_2O_3 > Pt_2/Fe_2O_3 > Pt_5/Fe_2O_3 > Pt_{10}/Fe_2O_3, again, in good agreement with the results from XPS measurements where both Pt^{2+} and Pt^{4+} species were found in the samples and the atomic ratio of Pt^{2+}/Pt^{4+} increased with increasing Pt loading (Figure 2a and Table S4). In addition, the fact that the absorption peak intensity also diminished from $Pt_{0.5}/Fe_2O_3$ to Pt_{10}/Fe_2O_3 (Figure 3b inset) is in line with the red shift of the Pt 4f binding energy observed in XPS measurements (Figure 2a and Table S4).

The corresponding Fourier transforms of the extended X-ray absorption fine structure (FT-EXAFS) spectra are shown in Figure 3c,d. All samples exhibited a prominent peak at ca. 1.45 Å in the Fe K-edge FT-EXAFS profiles (Figure 3c) due to the Fe−O path, which is consistent with that of commercial Fe_2O_3.[38] The samples also exhibited a minor peak at around 2.78 Å that was somewhat longer than that observed with commercial Fe_2O_3 (2.66 Å) for the Fe−Fe path, likely due to the amorphous structure of the samples.[39] For the Pt L_3-edge FT-EXAFS (Figure 3d), a major peak at ca. 1.57 Å can be identified for the two samples with a low Pt loading, $Pt_{0.5}/Fe_2O_3$ and Pt_1/Fe_2O_3, which can be ascribed to the Pt−O path.[40] However, with an increase in the Pt loading, an additional peak appeared at 1.89 Å with Pt_2/Fe_2O_3 and became

https://doi.org/10.1021/acs.jpcc.2c09033
J. Phys. Chem. C 2023, 127, 3996−4005

the dominant feature in Pt_5/Fe_2O_3 and Pt_{10}/Fe_2O_3, which most likely arose from the Pt−Cl path.[41] This is in good agreement with results from XPS measurements where the contents of Cl residuals increased from $Pt_{0.5}/Fe_2O_3$ to Pt_{10}/Fe_2O_3 and the Cl residuals were mostly bonded to Pt (Table S2).

Such a dynamic evolution of the atomic configurations can also be manifested in the corresponding wavelet transforms (WT) using commercial Fe_2O_3 and PtO_2 as the references (Figure S15). From the WT-EXAFS of the Fe K-edge spectra (Figure 3e and Figures S16 and S17a−S20a), only the first-shell Fe−O can be identified in all samples at (3.38 $Å^{-1}$, 1.32 Å). However, for the WT-EXAFS of the Pt L_3-edge profiles, $Pt_{0.5}/Fe_2O_3$ (Figure S17b) and Pt_1/Fe_2O_3 (Figure S18b) can be seen to exhibit only the first-shell Pt−O at (3.16 $Å^{-1}$, 1.47 Å) and both Pt−O and Pt−Cl (4.71 $Å^{-1}$, 1.69 Å) can be resolved in Pt_2/Fe_2O_3 (Figure S19b), whereas for Pt_5/Fe_2O_3 (Figure 3f) and Pt_{10}/Fe_2O_3 (Figure S20b), the Pt−Cl scattering now becomes the dominant feature. It is worth noting that no significant metal−metal scattering can be found in the WT-EXAFS spectra, in good agreement with the amorphous nature of the Fe_2O_3 scaffold and atomic dispersion of Pt within the matrix.

The fitting results of the Fe K-edge and Pt L_3-edge FT-EXAFS spectra of the sample series are listed in Figures S21−S22 and Table S6. The coordination number (CN) of the first-shell Fe−O remained rather consistent for the series of samples at 3.2 to 4.5, which is slightly lower than that of pristine hematite (Table S6). Concurrently, the CN of Pt−O was estimated to be 3.6 for $Pt_{0.5}/Fe_2O_3$ and diminished to 2.8 for Pt_1/Fe_2O_3, 1.9 for Pt_2/Fe_2O_3, and 1.2 for Pt_5/Fe_2O_3, whereas for Pt_{10}/Fe_2O_3, no Pt−O can be resolved. In contrast, the CN of Pt−Cl increased from ca. 1.2 for $Pt_{0.5}/Fe_2O_3$ to 1.5 for Pt_1/Fe_2O_3, 2.8 for Pt_2/Fe_2O_3, 3.6 for Pt_5/Fe_2O_3, and 4.4 for Pt_{10}/Fe_2O_3. This is in excellent agreement with the dynamic transition observed above from Pt−O to Pt−Cl as the Pt loading was increased. Note that no Pt−Fe path could be resolved from the data, implying that the Pt species were most probably attached to the surface of the Fe_2O_3 scaffold rather than embedded in the Fe_2O_3 crystal lattice. Figure 3g,h depicts the ball-and-stick structural models for Fe_2O_3 and Pt_5/Fe_2O_3, respectively.

Taken together, these results show that at low Pt loadings (i.e., $Pt_{0.5}/Fe_2O_3$ and Pt_1/Fe_2O_3), the samples consisted primarily of Fe_2O_3 decorated with individual Pt centers with minimal Cl residuals, whereas at higher Pt loadings (i.e., Pt_2/Fe_2O_3, Pt_5/Fe_2O_3, and Pt_{10}/Fe_2O_3), $PtCl_x$ species became increasingly dominant, likely due to the incomplete decomposition of the $PtCl_4$ precursor, and exerted significant impacts on the HER activity, as manifested below.

The Pt/Fe_2O_3 samples exhibited remarkable activity toward HER in acidic media. Figure 4a shows the polarization curves of the various nanocomposites in 0.5 M H_2SO_4, where upon the negative sweeping of the electrode potential, nonzero cathodic currents started to appear, suggesting apparent electrocatalytic activity toward HER. However, the activity varied markedly among the samples. For instance, one can see that the Pt-free Fe_2O_3 exhibited only minimal activity, with a high η_{10} of −660 mV. Upon the incorporation of Pt into the Fe_2O_3, the activity increased significantly, where η_{10} decreased drastically to −221 mV for $Pt_{0.5}/Fe_2O_3$, −60 mV for Pt_1/Fe_2O_3, −22 mV for Pt_2/Fe_2O_3, −15 mV for Pt_5/Fe_2O_3, and −24 mV for Pt_{10}/Fe_2O_3. Remarkably, the last three samples even outperformed commercial Pt/C (−34 mV).

Notably, in CV measurements (Figure S23), none of the samples showed any voltammetric profile that resembled the conventional butterfly feature arising from hydrogen adsorption/desorption on a platinum domain,[42,43] consistent with results from the above microscopic and spectroscopic measurements that Pt was most likely atomically dispersed on the Fe_2O_3 scaffold. In addition, the fact that Pt_5/Fe_2O_3 exhibited the most prominent voltammetric currents of hydrogen adsorption and desorption close to 0 V was likely due to the high electrical conductivity as suggested in the VBM measurements.

Consistent results were obtained from the analysis and comparison of the mass activity by normalizing the HER current to the Pt mass. From Figure 4b, at an overpotential of −50 mV, Pt_5/Fe_2O_3 exhibited a mass activity of 8.12 A mg_{Pt}^{-1}, greatly surpassing those of $Pt_{0.5}/Fe_2O_3$ (0.43 A mg_{Pt}^{-1}), Pt_1/Fe_2O_3 (1.52 A mg_{Pt}^{-1}), Pt_2/Fe_2O_3 (5.29 A mg_{Pt}^{-1}), and Pt_{10}/Fe_2O_3 (4.61 A mg_{Pt}^{-1}). In fact, the mass activity of Pt_5/Fe_2O_3 was about 4 times that of commercial Pt/C (2.17 A mg_{Pt}^{-1}), and the turnover frequency (TOF, details in the Supporting Information) of Pt_5/Fe_2O_3 was estimated to be ca. 0.15 and 6.57 s^{-1} at overpotentials of −10 and −50 mV, respectively, drastically higher than those of Pt/C (0.02 and 1.75 s^{-1}) (Figure S24).

The Tafel plots are shown in Figure 4c, where Pt_5/Fe_2O_3 exhibits a slope of 25.4 mV dec^{-1}, significantly lower than those of others in the series, $Pt_{0.5}/Fe_2O_3$ (135.8 mV dec^{-1}), Pt_1/Fe_2O_3 (40.4 mV dec^{-1}), Pt_2/Fe_2O_3 (26.8 mV dec^{-1}), Pt_{10}/Fe_2O_3 (27.6 mV dec^{-1}), and even Pt/C (25.9 mV dec^{-1}). This suggests facile electron-transfer kinetics of HER on Pt_5/Fe_2O_3. Indeed, from the Nyquist plots in Figure 4f and Figure S25, Pt_5/Fe_2O_3 can be seen to possess a charge-transfer resistance (R_{ct} = 1.28 Ω) at an overpotential of −10 mV that was drastically lower than those of the other samples, $Pt_{0.5}/Fe_2O_3$ (1960 Ω), Pt_1/Fe_2O_3 (55.50 Ω), Pt_2/Fe_2O_3 (11.70 Ω), Pt_{10}/Fe_2O_3 (3.94 Ω), and Pt/C (1.36 Ω) (Table S7). Taken together, these results indicate that Pt_5/Fe_2O_3 stood out as the best HER catalyst in the series. In fact, Pt_5/Fe_2O_3 even outperforms a number of state-of-the-art Pt-based electrocatalysts (Figure 4d and Table S8), such as PtRu/RFCS-6h (η_{10} = −19.7 mV),[44] Pt-PVP/TNR/GC (−21 mV),[45] and Pt-SA/ML-WO_3 (−22 mV).[18]

Notably, Pt_5/Fe_2O_3 also exhibited excellent durability in acidic media. From Figure 4e, it can be seen that η_{10} decayed by only 4 mV after 5000 cycles between −0.05 and 0 V. In fact, the chronoamperometric measurements (Figure 4e inset) exhibited virtually no decay during 10 h of continuous operation at an overpotential of −40 mV. (The diminishment of the voltammetric currents was due to the generation of H_2 bubbles that blocked the electrode surface, and almost 100% of the current was recovered once the bubbles were shaken off.)

Additionally, as shown in Figures S26−S31, the double-layer capacitance (C_{dl}) can be found to increase from 0.070 mF cm^{-2} for Fe_2O_3 to 0.130 mF cm^{-2} for $Pt_{0.5}/Fe_2O_3$, 0.117 mF cm^{-2} for Pt_1/Fe_2O_3, 0.145 mF cm^{-2} for Pt_2/Fe_2O_3, 0.499 mF cm^{-2} for Pt_5/Fe_2O_3, and 0.676 mF cm^{-2} for Pt_{10}/Fe_2O_3. This suggests an apparent increase in the electrochemically accessible surface area, likely due to the enhanced electrical conductivity of the samples by Pt modification, as suggested in the XPS and EIS measurements presented above.

https://doi.org/10.1021/acs.jpcc.2c09033
J. Phys. Chem. C 2023, 127, 3996−4005

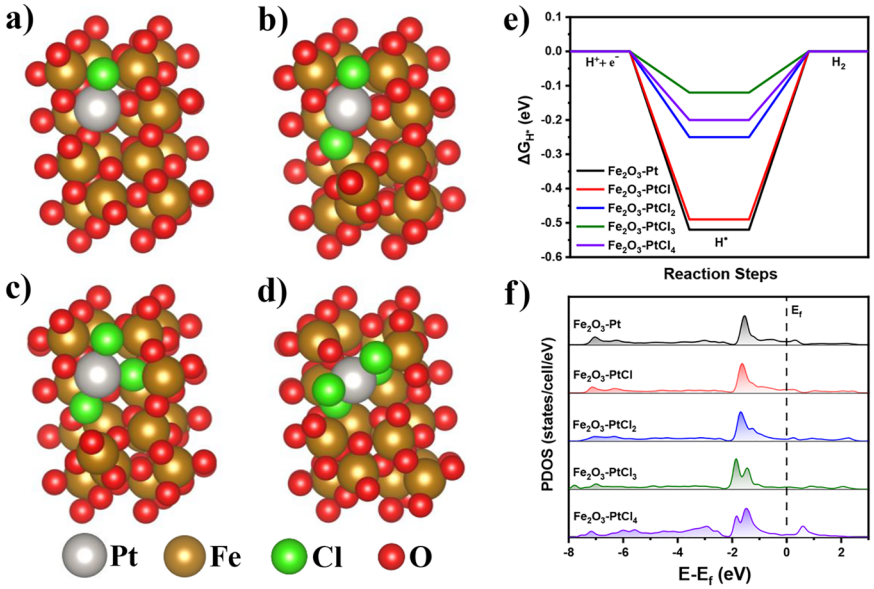

Figure 5. Structural models of a hematite Fe_2O_3 slab functionalized with (a) PtCl, (b) $PtCl_2$, (c) $PtCl_3$, and (d) $PtCl_4$. (e) Gibbs free energy of H* (ΔG_{H^*}) adsorption on the various models. (f) Projected density of states (PDOS) of the d electrons of Pt active sites in the various models.

To unravel the electrocatalytic mechanism, DFT calculations (details in the Supporting Information) were carried out with structural models based on a hematite slab functionalized with various $PtCl_x$ species, as suggested in the above experimental characterizations. Notably, when a Pt atom was anchored onto Fe_2O_3 with no Cl residual (Fe_2O_3−Pt) (Figure S32), the Gibbs free energy of H adsorption (ΔG_{H^*}, Figure S33a) was estimated to be −0.52 eV (Figure 5e), yet with the anchoring of PtCl onto the hematite surface (Fe_2O_3−PtCl, Figure 5a,e and Figure S33b), ΔG_{H^*} decreased to −0.49 eV and further to −0.25 eV for Fe_2O_3−$PtCl_2$ (Figure 5b,e and Figure S33c), −0.12 eV for Fe_2O_3−$PtCl_3$ (Figure 5c,e and Figure S33d), and −0.20 eV for Fe_2O_3−$PtCl_4$ (Figure 5d,e and Figure S33e). As a $|\Delta G_{H^*}|$ close to zero is preferred for HER electrocatalysis,[21,46] this suggests that the HER activity can be markedly enhanced by the Cl residuals, and Fe_2O_3−$PtCl_3$ represents the optimal configuration. This is in excellent agreement with the electrochemical performance described above.

The projected density of states (PDOS) of the Pt 3d electrons was then calculated to better understand the electronic configuration and interactions between the Pt atom and its coordination environment. From Figure 5f, it can be seen that the highest PDOS peak shifted from −1.54 eV for Fe_2O_3−Pt to −1.63 eV for Fe_2O_3−PtCl, −1.67 eV for Fe_2O_3−$PtCl_2$, and −1.85 eV for Fe_2O_3−$PtCl_3$ and bounced back to −1.49 eV for Fe_2O_3−$PtCl_4$. That is, among the series, Fe_2O_3−$PtCl_3$ possessed a PDOS distribution the farthest away from the Fermi level (E_f), which is anticipated to weaken H adsorption and facilitate H_2 desorption. Such a shift of the PDOS peak is likely due to p−d hybridization between the Cl and Pt elections (Figure S34). By contrast, a higher Cl coordination (i.e., Fe_2O_3−$PtCl_4$) would delocalize the Pt d electrons and render a significant splitting of the Pt d orbitals and generation of a new highest PDOS peak that is closer to E_f (Figure S35), according to crystal-field theory.[47,48] Therefore, too high a Cl coordination is not beneficial for H adsorption (additional contributions may arise from steric hindrance), as suggested in the above ΔG_{H^*} analysis. Furthermore, the number of Pt 5d electrons can be quantitatively assessed by the integration of the PDOS of the Pt 5d orbitals $\int_{-\infty}^{(E_f)} n_d(E)\,dE$, where $n_d(E)$ is the function of the density of states),[49] which increases from 8.26 for Fe_2O_3−Pt to 8.41 for Fe_2O_3−PtCl, 8.53 for Fe_2O_3−$PtCl_2$, 8.67 for Fe_2O_3−$PtCl_3$, and 8.62 for Fe_2O_3−$PtCl_4$ (Table S9). This suggests charge transfer from the residual Cl to Pt, which is consistent with the diminishing (increasing) binding energy of the Pt 4f (Cl 2p) electrons, as observed in XPS measurements (Figure 2), and the increasing content of Pt^{2+} ($5d^8$) species (Table S2).

CONCLUSIONS

A series of Pt-anchored Fe_2O_3 nanostructures were readily prepared by the thermal annealing of MIL-101 along with the addition of a controlled amount of $PtCl_4$. TEM and spectroscopic measurements suggested the formation of a largely amorphous Fe_2O_3 scaffold with nanocrystalline domains, and the Pt species were most likely atomically dispersed onto the Fe_2O_3 surface in the form of $PtCl_x$. It was found that the loading of Pt into the samples led to a marked change in the electronic properties, with the Pt_5/Fe_2O_3 sample behaving like a conductor whereas the rest behaved as semiconductors. Electrochemically, the Pt_5/Fe_2O_3 sample was found to exhibit the best HER activity in acidic media, with a performance at least 4 times better than that of commercial Pt/C, due to the unique VBM that facilitated electron-transfer reactions, as manifested in EIS and CV measurements. Results from DFT calculations showed that the anchoring of the $PtCl_x$ species onto the Fe_2O_3 surface significantly diminished $|\Delta G_{H^*}|$, with Fe_2O_3−$PtCl_3$ being the optimal configuration, among the series, where charge transfer from the Cl species to Pt weakened H adsorption, due to p−d hybridization between the Cl and Pt electrons. Results from this study highlight the enormous potential of metal oxides in the rational design and engineering of high-performance catalysts for electrochemical energy technologies and the impacts of anionic residuals on the electrocatalytic performance.

https://doi.org/10.1021/acs.jpcc.2c09033
J. Phys. Chem. C 2023, 127, 3996−4005

■ ASSOCIATED CONTENT

Supporting Information

The Supporting Information is available free of charge at https://pubs.acs.org/doi/10.1021/acs.jpcc.2c09033.

Additional experimental details and data; TOF calculations; methods of computational study; XRD patterns; additional TEM images, EDS and elemental maps; Raman spectra; additional XPS spectra; XAS data and fitting results; additional electrochemical data; structures for computational studies; DOS and PDOS plots; table summary of the fitting results of XPS and XAS data; comparison of HER activity with literature results; and number of electrons in Pt 5d orbitals from DFT calculations (PDF)

■ AUTHOR INFORMATION

Corresponding Author

Shaowei Chen − *Department of Chemistry and Biochemistry, University of California, Santa Cruz, California 95064, United States;* orcid.org/0000-0002-3668-8551; Email: shaowei@ucsc.edu

Authors

Bingzhe Yu − *Department of Chemistry and Biochemistry, University of California, Santa Cruz, California 95064, United States*

Qiming Liu − *Department of Chemistry and Biochemistry, University of California, Santa Cruz, California 95064, United States;* orcid.org/0000-0001-5839-5453

Forrest Nichols − *Department of Chemistry and Biochemistry, University of California, Santa Cruz, California 95064, United States*

Kiley Mayford − *Department of Physics, University of California, Santa Cruz, California 95064, United States*

Dingjie Pan − *Department of Chemistry and Biochemistry, University of California, Santa Cruz, California 95064, United States*

Han-Lin Kuo − *School of Engineering, University of California, Merced, California 95343, United States*

Jennifer Q. Lu − *School of Engineering, University of California, Merced, California 95343, United States;* orcid.org/0000-0002-1716-0380

Frank Bridges − *Department of Physics, University of California, Santa Cruz, California 95064, United States*

Complete contact information is available at: https://pubs.acs.org/10.1021/acs.jpcc.2c09033

Notes

The authors declare no competing financial interest.

■ ACKNOWLEDGMENTS

This work was supported by the National Science Foundation (CHE-1900235 and CHE-2003685). TEM, XPS, and Raman measurements were performed as part of a user project at the National Center for Electron Microscopy and Molecular Foundry, Lawrence Berkeley National Laboratory, which was supported by the Office of Science, Office of Basic Energy Sciences, U.S. Department of Energy under contract no. DE-AC02-05CH11231. XAS work was carried out at the Stanford Synchrotron Radiation Lightsource (SSRL), which is supported by the U.S. Department of Energy, Office of Science, Office of Basic Energy Sciences under contract no. DE-AC02-76SF00515. We thank Mr. J. Barnett for assistance with sample preparation and data collection for the XRD experiments and the X-ray Facility at the University of California Santa Cruz for the use of the Rigaku Smartlab diffractometer, funded by the National Science Foundation (MRI-1126845). Computational work was carried out using the UCSC Lux Supercomputer which is funded by the NSF MRI program (AST-1828315).

■ REFERENCES

(1) Hosseini, S. E.; Wahid, M. A. Hydrogen production from renewable and sustainable energy resources: Promising green energy carrier for clean development. *Renew Sust Energy Rev.* **2016**, *57*, 850−866.

(2) Sun, J. W.; Xu, W. J.; Lv, C. X.; Zhang, L. J.; Shakouri, M. S.; Peng, Y. H.; Wang, Q. Q.; Yang, X. F.; Yuan, D.; Huang, M. H.; Hu, Y. F.; Yang, D. J.; Zhang, L. X. Co/MoN hetero-interface nanoflake array with enhanced water dissociation capability achieves the Pt-like hydrogen evolution catalytic performance. *Appl. Catal. B: Environ* **2021**, *286*, 119882.

(3) Li, X.; Takano, S.; Tsukuda, T. Ligand Effects on the Hydrogen Evolution Reaction Catalyzed by Au-13 and Pt@Au-12: Alkynyl vs Thiolate. *J. Phys. Chem. C* **2021**, *125* (42), 23226−23230.

(4) Xue, Q.; Bai, X. Y.; Zhao, Y.; Li, Y. N.; Wang, T. J.; Sun, H. Y.; Li, F. M.; Chen, P.; Jin, P. J.; Yin, S. B.; Chen, Y. Au core-PtAu alloy shell nanowires for formic acid electrolysis. *J. Energy Chem.* **2022**, *65*, 94−102.

(5) Cai, J. L.; Ding, J.; Wei, D. H.; Xie, X.; Li, B. J.; Lu, S. Y.; Zhang, J. M.; Liu, Y. S.; Cai, Q.; Zang, S. Q. Coupling of Ru and O-Vacancy on 2D Mo-Based Electrocatalyst Via a Solid-Phase Interface Reaction Strategy for Hydrogen Evolution Reaction. *Adv. Energy Mater.* **2021**, *11* (26), 2100141.

(6) Dai, J.; Zhu, Y. L.; Chen, Y.; Wen, X.; Long, M. C.; Wu, X. H.; Hu, Z. W.; Guan, D. Q.; Wang, X. X.; Zhou, C.; Lin, Q.; Sun, Y. F.; Weng, S. C.; Wang, H. T.; Zhou, W.; Shao, Z. P. Hydrogen spillover in complex oxide multifunctional sites improves acidic hydrogen evolution electrocatalysis. *Nat. Commun.* **2022**, *13* (1), 1189.

(7) Du, H. F.; Du, Z. Z.; Wang, T. F.; Li, B. X.; He, S.; Wang, K.; Xie, L. H.; Ai, W.; Huang, W. Unlocking Interfacial Electron Transfer of Ruthenium Phosphides by Homologous Core-Shell Design toward Efficient Hydrogen Evolution and Oxidation. *Adv. Mater.* **2022**, *34* (37), 2204624.

(8) Wang, Z. B.; Tang, M. T.; Cao, A.; Chan, K.; Norskov, J. K. Insights into the Hydrogen Evolution Reaction on 2D Transition-Metal Dichalcogenides. *J. Phys. Chem. C* **2022**, *126* (11), 5151−5158.

(9) Shen, L. F.; Lu, B. A.; Qu, X. M.; Ye, J. Y.; Zhang, J. M.; Yin, S. H.; Wu, Q. H.; Wang, R. X.; Shen, S. Y.; Sheng, T.; Jiang, Y. X.; Sun, S. G. Does the oxophilic effect serve the same role for hydrogen evolution/oxidation reaction in alkaline media? *Nano Energy* **2019**, *62*, 601−609.

(10) Tang, T.; Ding, L.; Yao, Z. C.; Pan, H. R.; Hu, J. S.; Wan, L. J. Synergistic Electrocatalysts for Alkaline Hydrogen Oxidation and Evolution Reactions. *Adv. Funct. Mater.* **2022**, *32* (2), 2107479.

(11) Cheng, N. C.; Stambula, S.; Wang, D.; Banis, M. N.; Liu, J.; Riese, A.; Xiao, B. W.; Li, R. Y.; Sham, T. K.; Liu, L. M.; Botton, G. A.; Sun, X. L. Platinum single-atom and cluster catalysis of the hydrogen evolution reaction. *Nat. Commun.* **2016**, *7*, 13638.

(12) Wang, T. T.; Wang, M.; Yang, H.; Xu, M. Q.; Zuo, C. D.; Feng, K.; Xie, M.; Deng, J.; Zhong, J.; Zhou, W.; Cheng, T.; Li, Y. G. Weakening hydrogen adsorption on nickel via interstitial nitrogen doping promotes bifunctional hydrogen electrocatalysis in alkaline solution (vol 12, pg 3522, 2019). *Energy Environ. Sci.* **2019**, *12* (12), 3611−3611.

(13) Ding, Y.; Cao, K. W.; He, J. W.; Li, F. M.; Huang, H.; Chen, P.; Chen, Y. Nitrogen-doped graphene aerogel-supported ruthenium nanocrystals for pH-universal hydrogen evolution reaction. *Chin. J. Catal.* **2022**, *43* (6), 1535−1543.

(14) Liu, Y. H.; Wang, Q. L.; Zhang, J. C.; Ding, J.; Cheng, Y. Q.; Wang, T.; Li, J.; Hu, F. X.; Yang, H. B.; Liu, B. Recent Advances in

Carbon-Supported Noble-Metal Electrocatalysts for Hydrogen Evolution Reaction: Syntheses, Structures, and Properties. *Adv. Energy Mater.* **2022**, *12* (28), 2200928.
(15) Wu, Y.; Wei, W.; Yu, R.; Xia, L.; Hong, X.; Zhu, J.; Li, J.; Lv, L.; Chen, W.; Zhao, Y.; Zhou, L.; Mai, L. Q. Anchoring Sub-Nanometer Pt Clusters on Crumpled PaperLike MXene Enables High Hydrogen Evolution Mass Activity. *Adv. Funct. Mater.* **2022**, *32*, 2110910.
(16) Kuang, P. Y.; Wang, Y. R.; Zhu, B. C.; Xia, F. J.; Tung, C. W.; Wu, J. S.; Chen, H. M.; Yu, J. G. Pt Single Atoms Supported on N-Doped Mesoporous Hollow Carbon Spheres with Enhanced Electrocatalytic H_2 Evolution Activity. *Adv. Mater.* **2021**, *33* (18), 2008599.
(17) Zhou, K. L.; Wang, Z. L.; Han, C. B.; Ke, X. X.; Wang, C. H.; Jin, Y. H.; Zhang, Q. Q.; Liu, J. B.; Wang, H.; Yan, H. Platinum single-atom catalyst coupled with transition metal/metal oxide heterostructure for accelerating alkaline hydrogen evolution reaction. *Nat. Commun.* **2021**, *12* (1), 3783.
(18) Wang, D. L.; Li, H. P.; Du, N.; Hou, W. G. Single Platinum Atoms Immobilized on Monolayer Tungsten Trioxide Nanosheets as an Efficient Electrocatalyst for Hydrogen Evolution Reaction. *Adv. Funct. Mater.* **2021**, *31* (23), 2009770.
(19) Cheng, X.; Li, Y. H.; Zheng, L. R.; Yan, Y.; Zhang, Y. F.; Chen, G.; Sun, S. R.; Zhang, J. J. Highly active, stable oxidized platinum clusters as electrocatalysts for the hydrogen evolution reaction. *Energy Environ. Sci.* **2017**, *10* (11), 2450−2458.
(20) Lu, B. Z.; Liu, Q. M.; Wang, C. Y.; Masood, Z.; Morris, D. J.; Nichols, F.; Mercado, R.; Zhang, P.; Ge, Q. F.; Xin, H. L. L.; Chen, S. W. Ultrafast Preparation of Nonequilibrium FeNi Spinels by Magnetic Induction Heating for Unprecedented Oxygen Evolution Electrocatalysis. *Research* **2022**, *2022*, 9756983.
(21) Liu, Q. M.; Lu, B. Z.; Nichols, F.; Ko, J.; Mercado, R.; Bridges, F.; Chen, S. W. Rapid preparation of carbon-supported ruthenium nanoparticles by magnetic induction heating for efficient hydrogen evolution reaction in both acidic and alkaline media. *SusMat* **2022**, *2*, 335−346.
(22) Liu, Q. M.; Chen, S. W. Ultrafast synthesis of electrocatalysts. *Trends Chem.* **2022**, *4* (10), 918−934.
(23) Tang, Y. J.; Zheng, H.; Wang, Y.; Zhang, W.; Zhou, K. Laser-Induced Annealing of Metal-Organic Frameworks on Conductive Substrates for Electrochemical Water Splitting. *Adv. Funct. Mater.* **2021**, *31* (31), 2102648.
(24) Liang, Y. C.; Hung, C. S. Design of Hydrothermally Derived Fe_2O_3 Rods with Enhanced Dual Functionality Via Sputtering Decoration of a Thin ZnO Coverage Layer. *Acs Omega* **2020**, *5* (26), 16272−16283.
(25) Zhao, K. N.; Wen, M. Y.; Dong, Y. F.; Zhang, L.; Yan, M. Y.; Xu, W. W.; Niu, C. J.; Zhou, L.; Wei, Q. L.; Ren, W. H.; Wang, X. P.; Mai, L. Q. Thermal Induced Strain Relaxation of 1D Iron Oxide for Solid Electrolyte Interphase Control and Lithium Storage Improvement. *Adv. Energy Mater.* **2017**, *7* (6), 1601582.
(26) Mo, R.; Liu, Q.; Li, H. X.; Yang, S.; Zhong, J. X. Photoelectrochemical water oxidation in α-Fe_2O_3 thin films enhanced by a controllable wet-chemical Ti-doping strategy and Co-Pi co-catalyst modification. *J. Mater. Sci.:Mater. Electron.* **2019**, *30* (24), 21444−21453.
(27) Alduhaish, O.; Ubaidullah, M.; Al-Enizi, A. M.; Alhokbany, N.; Alshehri, S. M.; Ahmed, J. Facile Synthesis of Mesoporous α-Fe_2O_3@g-C_3N_4-NCs for Efficient Bifunctional Electro-catalytic Activity (OER/ORR). *Sci. Rep.* **2019**, *9*, 14139.
(28) Mansour, H.; Letifi, H.; Bargougui, R.; De Almeida-Didry, S.; Negulescu, B.; Autret-Lambert, C.; Gadri, A.; Ammar, S. Structural, optical, magnetic and electrical properties of hematite (α-Fe_2O_3) nanoparticles synthesized by two methods: polyol and precipitation. *Appl. Phys. A: Mater.* **2017**, *123* (12), 787.
(29) Sapnar, K. P. J.; Gawali, S. R. Synthesis and Raman study of iron oxide nanoparticles. *Compliance Engineering Journal* **2019**, *10* (11), 382−390.
(30) Nichols, F.; Liu, Q. M.; Sandhu, J.; Azhar, Z.; Cazares, R.; Mercado, R.; Bridges, F.; Chen, S. W. Platinum-complexed phosphorous-doped carbon nitride for electrocatalytic hydrogen evolution. *J. Mater. Chem. A* **2022**, *10* (11), 5962−5970.
(31) Nichols, F.; Lu, J. E.; Mercado, R.; Dudschus, R.; Bridges, F.; Chen, S. W. Platinum Oxide Nanoparticles for Electrochemical Hydrogen Evolution: Influence of Platinum Valence State. *Chem.—Eur. J.* **2020**, *26* (18), 4136−4142.
(32) Rajan, A.; Sharma, M.; Sahu, N. K. Assessing magnetic and inductive thermal properties of various surfactants functionalised Fe_3O_4 nanoparticles for hyperthermia. *Sci. Rep.* **2020**, *10* (1), 15045.
(33) Zhao, Y. X.; Lai, Q. X.; Wang, Y.; Zhu, J. J.; Liang, Y. Y. Interconnected Hierarchically Porous Fe, N-Codoped Carbon Nanofibers as Efficient Oxygen Reduction Catalysts for Zn-Air Batteries. *ACS Appl. Mater. Interfaces* **2017**, *9* (19), 16178−16186.
(34) Li, C. F.; Zhao, J. W.; Xie, L. J.; Wu, J. Q.; Li, G. R. Fe doping and oxygen vacancy modulated Fe-Ni_5P_4/NiFeOH nanosheets as bifunctional electrocatalysts for efficient overall water splitting. *Appl. Catal. B: Environ* **2021**, *291*, 119987.
(35) Li, G. K.; Jang, H.; Liu, S. G.; Li, Z. J.; Kim, M. G.; Qin, Q.; Liu, X.; Cho, J. The synergistic effect of Hf-O-Ru bonds and oxygen vacancies in Ru/HfO_2 for enhanced hydrogen evolution. *Nat. Commun.* **2022**, *13* (1), 1270.
(36) Liu, R.; Tonjes, W. C.; Greanya, V. A.; Olson, C. G.; Frindt, R. F. Fermi surface of 2H-TaSe2 and its relation to the charge-density wave. *Phys. Rev. B* **2000**, *61* (8), 5212−5216.
(37) Peng, Y.; Liu, Q. M.; Lu, B. Z.; He, T.; Nichols, F.; Hu, X.; Huang, T.; Huang, G.; Guzman, L.; Ping, Y.; Chen, S. W. Organically Capped Iridium Nanoparticles as High-Performance Bifunctional Electrocatalysts for Full Water Splitting in Both Acidic and Alkaline Media: Impacts of Metal-Ligand Interfacial Interactions. *ACS Catal.* **2021**, *11* (3), 1179−1188.
(38) Gu, H. Y.; Liu, X.; Liu, X. F.; Ling, C. C.; Wei, K.; Zhan, G. M.; Guo, Y. B.; Zhang, L. Z. Adjacent single-atom irons boosting molecular oxygen activation on MnO2. *Nat. Commun.* **2021**, *12* (1), 5422.
(39) Yang, H.; Gong, L. Q.; Wang, H. M.; Dong, C. L.; Wang, J. L.; Qi, K.; Liu, H. F.; Guo, X. P.; Xia, B. Y. Preparation of nickel-iron hydroxides by microorganism corrosion for efficient oxygen evolution. *Nat. Commun.* **2020**, *11* (1), 5075.
(40) Friebel, D.; Miller, D. J.; O'Grady, C. P.; Anniyev, T.; Bargar, J.; Bergmann, U.; Ogasawara, H.; Wikfeldt, K. T.; Pettersson, L. G. M.; Nilsson, A. In situ X-ray probing reveals fingerprints of surface platinum oxide. *Phys. Chem. Chem. Phys.* **2011**, *13* (1), 262−266.
(41) Tang, P.; Lee, H. J.; Hurlbutt, K.; Huang, P. Y.; Narayanan, S.; Wang, C. B.; Gianolio, D.; Arrigo, R.; Chen, J.; Warner, J. H.; Pasta, M. Elucidating the Formation and Structural Evolution of Platinum Single-Site Catalysts for the Hydrogen Evolution Reaction. *ACS Catal.* **2022**, *12* (5), 3173−3180.
(42) He, G. Q.; Song, Y.; Liu, K.; Walter, A.; Chen, S.; Chen, S. W. Oxygen Reduction Catalyzed by Platinum Nanoparticles Supported on Graphene Quantum Dots. *ACS Catal.* **2013**, *3* (5), 831−838.
(43) He, Q. G.; Yang, X. F.; Chen, W.; Mukerjee, S.; Koel, B.; Chen, S. W. Influence of phosphate anion adsorption on the kinetics of oxygen electroreduction on low index Pt(hkl) single crystals. *Phys. Chem. Chem. Phys.* **2010**, *12* (39), 12544−12555.
(44) Li, K.; Li, Y.; Wang, Y. M.; Ge, J. J.; Liu, C. P.; Xing, W. Enhanced electrocatalytic performance for the hydrogen evolution reaction through surface enrichment of platinum nanoclusters alloying with ruthenium in situ embedded in carbon. *Energy Environ. Sci.* **2018**, *11* (5), 1232−1239.
(45) Li, C.; Chen, Z.; Yi, H.; Cao, Y.; Du, L.; Hu, Y. D.; Kong, F. P.; Campen, R. K.; Gao, Y. Z.; Du, C. Y.; Yin, G. P.; Zhang, I. Y.; Tong, Y. J. Polyvinylpyrrolidone-Coordinated Single-Site Platinum Catalyst Exhibits High Activity for Hydrogen Evolution Reaction. *Angew. Chem., Int. Ed.* **2020**, *59* (37), 15902−15907.
(46) Lu, B. Z.; Guo, L.; Wu, F.; Peng, Y.; Lu, J. E.; Smart, T. J.; Wang, N.; Finfrock, Y. Z.; Morris, D.; Zhang, P.; Li, N.; Gao, P.; Ping, Y.; Chen, S. W. Ruthenium atomically dispersed in carbon outperforms platinum toward hydrogen evolution reaction in alkaline media. *Nat. Commun.* **2019**, *10*, 631.

https://doi.org/10.1021/acs.jpcc.2c09033
J. Phys. Chem. C 2023, 127, 3996−4005

(47) Li, F. F.; Niu, Z. P.; Zhang, L. X. Monolayer 1T and 1T ' MoSO as Promising Electrocatalyst for Hydrogen Evolution based on First Principle Calculations. *ChemPhysChem* **2021**, *22* (19), 2034−2041.
(48) Ai, X.; Zou, X.; Chen, H.; Su, Y. T.; Feng, X. L.; Li, Q. J.; Liu, Y. P.; Zhang, Y.; Zou, X. X. Transition-Metal-Boron Intermetallics with Strong Interatomic d-sp Orbital Hybridization for High-Performance Electrocatalysis. *Angew. Chem., Int. Ed.* **2020**, *59* (10), 3961−3965.
(49) Nørskov, J. K.; Studt, F.; Abild-Pedersen, F.; Bligaard, T. *Fundamental Concepts in Heterogeneous Catalysis*; John Wiley & Sons: 2014.

https://doi.org/10.1021/acs.jpcc.2c09033
J. Phys. Chem. C 2023, 127, 3996−4005